Multidimensional Ripple Correlation Technique for Optimal Operation of Triple-Active-Bridge Converters

Ahmed A. Ibrahim ⊙, *Student Member, IEEE*, Tommaso Caldognetto ⊙, *Senior Member, IEEE*, Davide Biadene ⊙, *Member, IEEE*, and Paolo Mattavelli ⊙, *Fellow, IEEE*

Abstract—**This article presents a multidimensional ripple correlation search technique of optimal operating points of triple-active-bridge (TAB) converters. Such converters present multiple modulation parameters that should be exploited to achieve high operation efficiency. On the other hand, the several degrees of freedom available make the identification of optimal parameters a challenging task, not easily tackled analytically or in closed form. A model-free online search method based on the ripple correlation technique is then proposed in this article. The proposed method finds the optimum modulation parameters of TAB converters utilizing a three-dimensional ripple correlation control. The key property of the proposed solution is the adoption of orthogonal perturbation signals, where the orthogonality is simply obtained using different injection frequencies. The multidimensional correlation technique originally shown herein can be applied to other generic optimization problems. The proposed search is verified through a hardware-in-the-loop validation setup and an experimental prototype rated 5 kW.**

Index Terms—**DC–DC converters, extremum seeking control search, isolated multiport converter, optimum switching patterns, ripple correlation control search, triple active bridge (TAB).**

I. INTRODUCTION

ISOLATED multiport converters (IMPCs) allow compact solutions with reduced number of components for the interconnection of multiple energy resources. This is valuable in several emerging applications, like, for example, home nanogrids and electrified vehicles [1], [2], [3], [4]. Effective IMPCs can be achieved by extending the concept of the dual-active-bridge

Fig. 1. (a) TAB converter. (b) PSM. (c) Penta PSM. Modulation variables $\phi_2, \phi_3, D_1, D_2, D_3$ highlighted.

(DAB) converter, that is, by utilizing a multiterminal high-frequency transformer to couple ports at different voltage levels [5], [6]. Adding one extra port to the DAB gives the triple-active-bridge (TAB) topology, which is one of the simplest IMPC topologies utilizing a three-terminal high-frequency transformer, as shown in Fig. 1(a) [7]. In order to control the power flow, magnitude, and direction, the phase-shift modulation (PSM) is commonly applied [see Fig. 1(b)]. By the PSM, the three full-bridges generate ac voltages v_1, v_2, v_3 with duty-cycle fixed at 50% and phase-shifts ϕ_2 and ϕ_3 regulated to achieve specific power flows among the ports [8], [9]. As a disadvantage of this kind of modulation, relatively high conduction and switching losses are typically observed while operating at light load or with significant voltage mismatches among the transformer terminals, that is, while far from the condition $V1 : V2 : V3 = n_1 : n_2 : n_3$. To overcome this limitation, penta PSM schemes have been proposed [10]. By such modulation schemes, represented in Fig. 1(c), also the duty-cycles D_1, D_2, D_3 of the three ports are modulated, with the aim of reducing the converter loss. Of course, the increased

number of modulation parameters increases the complexity of the approach.

It can be shown that with five modulation parameters D_1, D_2, D_3, ϕ_2, and ϕ_3 the employed three full-bridges can generate 720 different voltage patterns, considering the number of permutations corresponding to the different sequences of rising and falling edges of v_1, v_2, and v_3 [5]. To analyze each switching pattern with the aim of finding optimum operation, for example, in terms of losses, may easily result unpractical. The literature describes different approaches reporting converter efficiency improvements [10], [11], [12], [13], [14], [15], [16], [17]. In [10], reduced power losses are achieved by modulating the duty-cycle and the phase-shift (penta phase-shift) based on fundamental component analysis (FCA) of the converter voltages and currents. While analyzes based on only the fundamental components are effective at moderate-to-high transferred power among the ports, the true power loss differs from the fundamental power loss at low-power levels, limiting the effectiveness of the approach. Moreover, fundamental analysis misses most of the insight into the shape of the switching patterns, which gives important information for switching loss reduction. A zero-voltage switching criterion for TAB has been introduced in [11], utilizing penta PSM, and taking into account all the parameters of the TAB converter, including the parasitic capacitance of the switches, the leakage inductance of the transformer, and the switching frequency. However, this approach introduced in [11] neglects conduction loss. In [12], a universal analytical model of the TAB converter is developed utilizing frequency domain analysis (FDA) and then exploited to pursue total loss reduction via particle-swarm optimization (PSO). The PSO searches for minimum rms current while fulfilling ZVS constraints. As in [10] and [11], Li et al. [12] employed a look-up table (LUT) to store the optimum modulation parameters preliminary calculated offline. In [13], a generalized harmonic approximation (GHA) model is developed for the TAB converter, which is then used in an online gradient-descent optimization aiming at minimizing the derived analytical model (AM) of the total rms current. The same approach is also presented in [14] and [15], optimizing the converter overall efficiency based on the GHA analysis.

In summary, a number of solutions are described in the literature for TAB converters efficiency improvements. The complexity of the optimization problem, stemming from the converter behavior and structure and the multiple degrees of freedom available for modulation, commonly brings to complex analytical results and optimization approaches that can barely achieve actual optimal operation. A different approach is proposed herein, in which optimal modulation parameters are pursued automatically by means of an online search method based on ripple correlation control (RCC). The proposed multidimensional correlation technique is model-free, endowing the approach with general validity. In fact, the proposed solution is effective regardless of TAB parameters variations during operation and can adapt modulation parameters automatically online. For example, the approach well tolerates partial or total uncertainties on the parameters of the used switches, parameters of the magnetics and passive components, controller and plant dynamics, etc. Such

TABLE I
COMPARISON WITH OTHER REPRESENTATIVE APPROACHES

Ref.	approach	online optimization	core implementation	optimized losses
[10]	FCA	✗	LUT	total
[11]	FDA	✗	LUT	switching
[12]	FDA	✗	LUT	total
[13]	GHA	✓	AM	conduction
[14], [15]	GHA	✓	AM	total
herein	model-free	✓	RCC	total

information is not needed to apply the approach successfully and may be left unknown. The feature just remarked extends the potential application of what presented herein to other similar optimization problems with multiple degrees of freedom. The features of the proposed method compared with other relevant approaches in the literature are summarized in Table I.

In the following, the online search technique based on RCC search method in a three-dimensional space (3D-RCC) is proposed and described to find the optimum duty-cycles for a given set-point of voltage and power levels at the ports of a TAB converter. Specifically, Section II provides the model of RCC establishing the central concept behind the proposed 3D-RCC. Section III presents the 3D-RCC considering the optimal operation of the TAB converter. Section IV discusses stability considerations of the proposed approach. Section V demonstrates the proposed 3D-RCC reporting hardware-in-the-loop (HIL) simulation results and experimental results. Finally, Section VI concludes this article.

II. RIPPLE CORRELATION CONTROL

One-dimensional RCC has been applied for photovoltaic maximum power point tracking [18], [19], [20]. In these applications, the RCC objective is to optimize a cost function $x(y)$, namely, the photovoltaic power, which is dependent on a state variable y, which is typically the panel voltage or current. The technique and related nomenclature are introduced in the following and then extended to the three-dimensional case applied to TAB optimization in Section III.

Given n samples $x(k-i)$, $y(k-i)$, $i = 1, \ldots, n$ of the couple of discrete-time variables $x(k)$, $y(k)$, their correlation can be described by the sample Pearson's correlation coefficient [21] as

$$\rho_{xy}(k) = \frac{\sum_{i=1}^{n} [x(k-i) - \bar{x}(k)] \cdot [y(k-i) - \bar{y}(k)]}{\sigma_x(k) \cdot \sigma_y(k)} \quad (1)$$

where σ_x, σ_y and $\bar{x}$, $\bar{y}$ are the sample standard deviations and means of x and y, respectively; for example, for variable x

$$\sigma_x(k) = \sqrt{\sum_{i=1}^{n} [x(k-i) - \bar{x}(k)]^2} \quad (2)$$

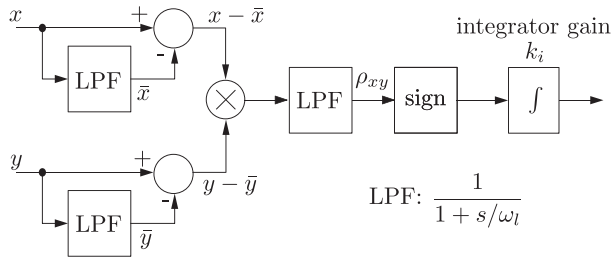$$\bar{x}(k) = \frac{1}{n} \sum_{i=1}^{n} x(k-i). \quad (3)$$

Fig. 2. One-dimensional RCC principle based on (4). LPF are used to approximate the mean operation.

Assume x represents a cost function and y a controllable variable. Three cases can be distinguished for the correlation coefficient in (1), namely, the following.

1) $\rho_{xy}(k) > 0$: A positive correlation between the variables x and y. This means that the controlled variable y should be reduced to reduce the cost function x.
2) $\rho_{xy}(k) < 0$: A negative correlation between variables x and y. This means that the controlled variable y should be increased to reduce the cost function x.
3) $\rho_{xy}(k) = 0$: No correlation between variables x and y.

The sign information is enough to describe the correlation between the two variables and decide how to modify the controllable variable y in order to reduce the cost x.

Remarkably, the sign information is solely carried by the numerator of (1), whilst the terms at the denominator are always positive, by definition. It yields

$$\text{sign}\left(\rho_{xy}(k)\right)$$
$$= \text{sign}\left(\sum_{i=1}^{n}\left[x(k-i)-\bar{x}(k)\right]\cdot\left[y(k-i)-\bar{y}(k)\right]\right) \quad (4)$$

Equation (4) can be represented in an approximate way as shown in Fig. 2, where the operation of mean (i.e., average) is implemented by means of low-pass filters (LPFs). In Fig. 2, the sign of the correlation coefficient $\rho_{xy}(k)$ is given as input to an integrator, whose output can used to adjust the value of the controllable variable y to result in lower values of x. For example, assume that the integrator output is used to decrease the value of y. Assume also that a positive correlation is found. In this case the output of the integrator increases and, due to the positive correlation among x and y, x decreases too, moving toward values of lower cost. Eventually, the previously remarked properties of the sign of ρ_{xy} indicate that if a local minimum is reached, the process finds an equilibrium point at that local minimum. In applications, the search is performed by analyzing how a small perturbation of given frequency superimposed to the controlled variable y correlates with the related changes on the cost variable x.

The theoretical framework behind the RCC is the perturbing extremum seeking control (ESC) theory, as referred to in the field of control systems engineering [22], [23]. ESC has been studied as an online control search for several fields distinct from power electronics with the same concepts of the RCC described above [24], [25], [26]. Its peculiarity is the property of being a model-free approach for optimization, which allows effective, low-complexity solutions.

The simple principle of RCC can be exploited for the search of optimal operating points even in case of complex systems, that is, relations among cost and controllable variables. The principle, just discussed in one-dimensional terms, as commonly found in the literature, is described in the following in a more general application that considers a three-dimensional problem for the optimization of a TAB converter. This is possible by performing the RCC search by using orthogonal perturbations for the controllable variables. Herein, it is shown the case of using perturbation signals at different frequencies, one for each controlled variable, and separately correlate the perturbation signals with the corresponding ones present in the cost variable.

III. EXTENSION TO 3D-RCC FOR TAB OPTIMIZATION

Consider now the problem of reducing the power loss of a TAB by searching for optimal modulation parameters. Consider also to pursue conduction loss minimization by applying an RCC search having as cost variable the total rms current

$$i^{\text{rms}} = \sqrt{\sum_{p=1}^{3} r_p \left(i_p^{\text{rms}}\right)^2} = f(\phi_2, \phi_3, D_1, D_2, D_3) \quad (5)$$

where weights r_p, $p = 1, \ldots, 3$, are the equivalent path resistances of the respective pth port. Notably, the total rms current depends on five modulation variables: two phase-shifts (i.e., ϕ_2, ϕ_3) plus three duty-cycles (i.e., D_1, D_2, D_3). In basic TAB controllers, the phase-shifts are used to regulate the voltages or the power exchanged among the ports [e.g., by proportional-integrative (PI) regulators], while the duty-cycles are kept fixed at 50%. Differently, more advanced modulators can exploit the three duty-cycles to optimize the converter operation [10], [27], [28]. Such optimization that exploits the degrees of freedom given by the duty-cycles is performed herein by the presented 3D-RCC approach.

The core concept of 3D-RCC is analogous to the RCC discussed in Section II, by splitting the three-dimensional problem, with the three variables D_1, D_2, D_3, into three separate problems, each considering a single variable. The separation can be done by employing the orthogonality principle, perturbing each duty-cycle with a different frequency, and evaluating the correlation between it and the cost function.

Three RCC searches can be performed concurrently by using corresponding perturbation signals at different frequencies

$$\epsilon \sin \omega_p t, \quad p = 1, \ldots, 3 \quad (6)$$

and by correlating the perturbations of same frequency found on the controllable and on the cost variables. Fig. 3 displays the resulting scheme. Each duty-cycle correlation search has a different frequency (i.e., ω_1, ω_2, and ω_3) with the same magnitude ϵ, chosen small with respect to the full duty-cycle. The forced disturbance of each duty-cycle is correlated separately to the total rms current positively or negatively. By tuning each duty-cycle value to the optimum value till the correlation result is equal to zero, that is, the minimum rms value is reached.
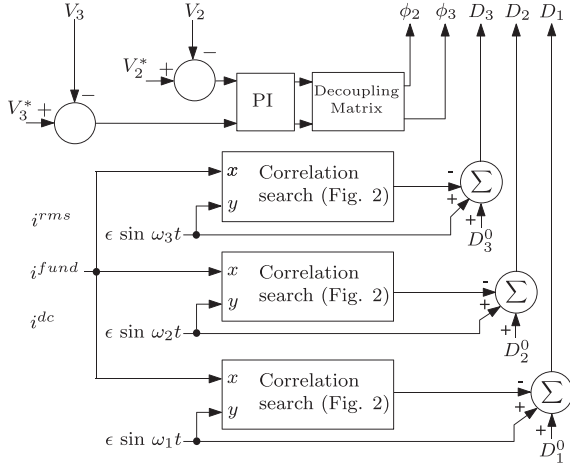
Fig. 3. 3D-RCC for searching optimal modulation variables ϕ_2, ϕ_3, D_1, D_2, D_3. Cost variables can be rms, fundamental, or dc currents.

In general, as highlighted in Fig. 3 and shown in Section V, different cost variables can be considered, like, for example, the input dc-current, the rms of the fundamental currents, or the total rms current.

As a final remark regarding the implementation of the voltage control-loops, a decoupling matrix, visibile in Fig. 3, is applied herein to slightly adjust the phase-shifts given the duty-cycles computed online. This control refinement was originally proposed in [10], which highlighted a coupling between the two voltage control loops and proposed the use of a decoupling matrix to decompose the multivariable control system into a series of independent, single-loop subsystems.

IV. STABILITY CONSIDERATIONS

While this article focuses on showing the application of the RCC in a multidimensional case in power electronics and presenting the solution to the TAB optimization problem by exploiting this model-free method, in the field of control-systems engineering other papers addressed the analyses and stability study of the class of ESC approaches, to which the 3D-RCC belongs [23], [24], [25], [26]. In addition to what was discussed in the previous sections, a set of constraints should be met to ensure a stable operation of the whole system. Once these conditions are satisfied, the method achieves convergence regardless of the specific converter parameters (e.g., kind of switching devices, amount of conduction loss, etc.), hence, its model-free property. Specifically, to guarantee stable operation of the proposed 3D-RCC, the following relations should be considered for parameters selection.

1) *Perturbation frequencies:* ω_1, ω_2, and ω_3 in (6) must be distinguishable, namely, orthogonal perturbation signals. Hereinafter, ω_M and ω_m indicate the maximum and minimum values, respectively, of the used perturbation frequencies.
2) *Dynamics of the plant to be optimized:* the maximum perturbation frequency ω_M should be much slower than the plant dynamics. This means that ω_M should lay well below the crossover frequency of the voltage controllers

(i.e., the PI regulators in Fig. 3). In our case, typical voltage controllers bandwidths are in the order of hundreds of hertz, then ω_M may be chosen an order of magnitude lower.
3) *LPF cut-off frequency:* the cut-off frequency of the LPF in Fig. 2 should be much lower than the minimum perturbing frequency ω_m, to well approximate the average operation in (4).
4) *Correlation integration gain:* the minimum perturbing frequency must be greater than the correlation integrator gain in Fig. 2, namely $\omega_m \gg k_i$. This means that the optimization variables D_1, D_2, and D_3 in Fig. 3 change slowly even with respect to the "slowest" perturbation signal, of frequency ω_m.
5) *Amplitude of perturbations:* the perturbations amplitude ϵ in (6) should be chosen to allow small variations around the optimal operating points (e.g., $\epsilon \simeq 1\%$ of full duty-cycle).
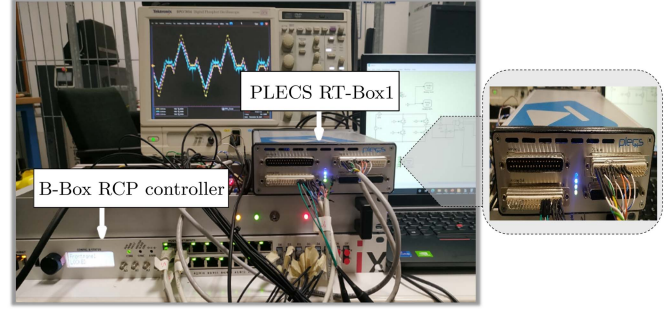

Fig. 4. HIL validation setup: PLECS RT-Box1 emulates converter operation, B-Box RCP controller implements the proposed 3D-RCC search.

V. VALIDATION RESULTS

In this section, the validation of the proposed 3D-RCC search is reported considering the results from an HIL setup and an experimental prototype. With the aim of demonstrating the effectiveness of the approach considering several different objectives (i.e., cost functions), the approach is demonstrated while considering total true rms current optimization, total fundamental rms current optimization, and input dc current optimization. The use of different validation tools (i.e., HIL and experimental prototype) and cost functions allows an accurate validation of the optimization approach and to show its robustness with respect to various implementations and cost functions.

A. HIL Validation

The real-time simulator PLECS RT-Box1, as shown in Fig. 4, has been used to model the TAB converter operation. The considered parameters are listed in Table II. The 3D-RCC search and converter control and modulation are implemented on an Imperix L.t.d. B-Box RCP controller. These first tests performed on an HIL platform allow to focus on the validation of the proposed technique when deployed in the final digital control platform interfaced to an emulated plant (i.e., TAB converter)

TABLE II
HIL VALIDATION PARAMETERS

Parameters		Value
Nominal power at each port P_{rated}	kW	5
Switching frequency $f_{sw} = 1/T_{sw}$	kHz	5
Rated dc voltages $V_1 = V_2 = V_3$	V	400
Transf. turns ratio $n_1 : n_2 : n_3$		1:1:1
Transf. leakage inductances:		
Port-1 leakage inductance L_1	μH	320
Port-2 leakage inductance L_2	μH	376
Port-3 leakage inductance L_3	μH	328
Sinusoidal disturbance magnitude ϵ		0.01
Sinusoidal disturbance-1 freq. ω_1	rad/s	24π
Sinusoidal disturbance-2 freq. ω_2	rad/s	20π
Sinusoidal disturbance-2 freq. ω_3	rad/s	16π
Simulation integration step T_{step}	μs	4

TABLE III
EXPERIMENTAL PROTOTYPE PARAMETERS

Parameters		Value
Nominal power at each port P_{rated}	kW	5
Switching frequency $f_{sw} = 1/T_{sw}$	kHz	40
Rated dc voltages $V_1 = V_2 = V_3$	V	400
Transf. turns ratio $n_1 : n_2 : n_3$		1:1:1
Transf. leakage inductances:		
Port-1 leakage inductance L_1	μH	40
Port-2 leakage inductance L_2	μH	47
Port-3 leakage inductance L_3	μH	41
Sinusoidal disturbance magnitude ϵ		0.01
Sinusoidal disturbance-1 freq. ω_1	rad/s	24π
Sinusoidal disturbance-2 freq. ω_2	rad/s	20π
Sinusoidal disturbance-2 freq. ω_3	rad/s	16π
Dead time	μs	1
Switching Devices		MMIX1Y100N120C3H1

that is free from parameters uncertainties and nonidealities. This simplifies the comparison with solutions obtained analytically or in simulation and to test the controller before being connected to the real-hardware. Given the fixed integration time step T_{step} (see Table II) possible with the adopted state-of-the-art emulator PLECS RT-Box1, a scaled-down switching frequency is considered with respect to the one used with the experimental prototype. This allowed us to have $T_{sw}/T_{step} = 50$ steps within a switching period and then to preserve sufficient accuracy of the obtained results. Of course, to keep the same current waveforms and, then, their rms, leakage inductance values are also scaled up by the same factor as the switching frequency (cf. Tables II and III).

In order to show the efficacy of the proposed 3D-RCC, the obtained results are compared with the results obtained by a brute-force (BF) search in which, given the voltage levels and the powers exchanged at the ports, the converter operation is systematically evaluated at all the points of a dense mesh of the space D_1, D_2, and D_3. On this basis, the results obtained by the BF search are regarded as the true optimum solutions.

Fig. 5 shows the obtained results at $V_1 = 400\,\mathrm{V}$, $V_2 = 320\,\mathrm{V}$, $V_3 = 480\,\mathrm{V}$, and $P_2 = 350\,\mathrm{W}$, while port-3 power
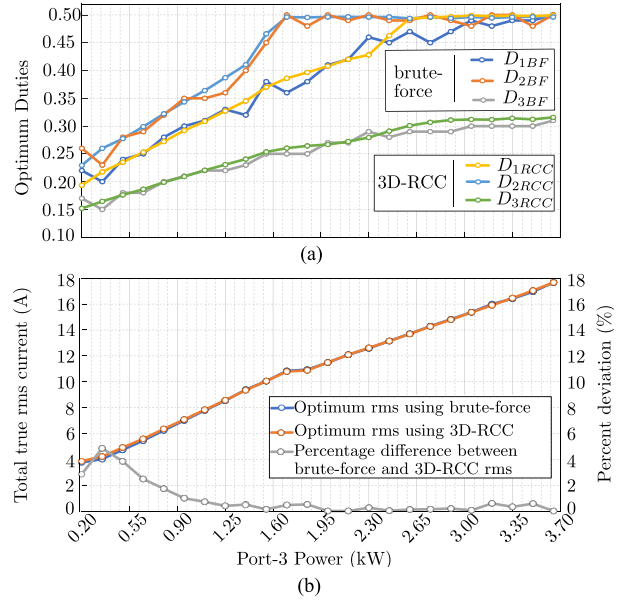
Fig. 5. HIL validation showing, for both BF and 3D-RCC search, (a) optimum duty-cycles versus power level, (b) total true rms current. Test conditions: $V_1 = 400\,\mathrm{V}$, $V_2 = 320\,\mathrm{V}$, $V_3 = 480\,\mathrm{V}$, $P_2 = 350\,\mathrm{W}$.
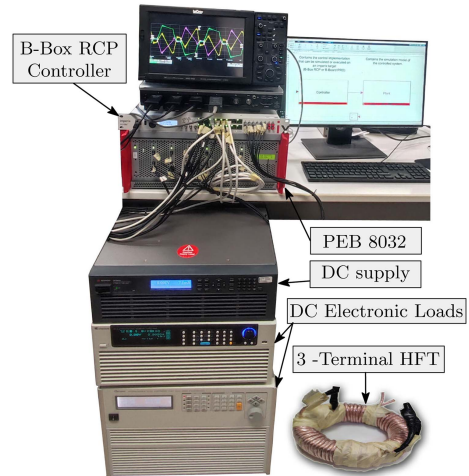
Fig. 6. Laboratory prototype of TAB with 3D-RCC.

P_3 is changing with $150\,\mathrm{W}$ step, with total true rms current (5) as optimization objective. Specifically, Fig. 5(a) shows the optimum duty-cycles found by the BF search (i.e., D_{1BF}, D_{2BF}, D_{3BF}) compared to the 3D-RCC search results (i.e., D_{1RCC}, D_{2RCC}, D_{3RCC}). The searching techniques give almost the same optimum duty cycles over the considered P_3 variation. Fig. 5(b) shows the total true rms currents corresponding to the BF search findings and 3D-RCC search findings, with the maximum deviation between the two currents of less than 5%.

B. Experimental Prototype Validation

The experimental prototype in Fig. 6, with parameters listed in Table III, has been implemented to verify the proposed three-dimensional correlation search. As shown in Fig. 7, port-1 of the converter is connected to a fixed dc-source $V_1 = 400\,\mathrm{V}$, port-2

TABLE IV
3D-RCC Search Optimal Results for Different Test Points (TP1-TP11), With $V_1 = 400$ V, $V_2 = 320$ V, $V_3 = 480$ V, $P_2 = 350$ W

| TP	P_3 (kW)	Optimizing true rms current (i^{rms})						Optimizing input dc current (i^{dc})						Optimizing fund. rms current (i^{fund})					
		D_1^{opt}	D_2^{opt}	D_3^{opt}	i^{rms} (A)	i^{dc} (A)	i^{fund} (A)	D_1^{opt}	D_2^{opt}	D_3^{opt}	i^{rms} (A)	i^{dc} (A)	i^{fund} (A)	D_1^{opt}	D_2^{opt}	D_3^{opt}	i^{rms} (A)	i^{dc} (A)	i^{fund} (A)
TP_1	0.20	0.210	0.230	0.145	4.20	1.59	3.10	0.212	0.239	0.113	4.85	1.57	3.76	0.257	0.298	0.178	4.50	1.62	2.96
TP_2	0.35	0.236	0.260	0.160	4.90	1.96	3.68	0.239	0.271	0.137	5.16	1.93	3.92	0.266	0.316	0.187	5.08	2.00	3.54
TP_3	0.50	0.258	0.282	0.178	5.54	2.35	4.35	0.259	0.302	0.155	5.69	2.33	4.40	0.276	0.326	0.190	5.72	2.40	4.23
TP_4	0.65	0.281	0.320	0.195	6.26	2.75	5.00	0.281	0.327	0.172	6.30	2.72	5.00	0.294	0.342	0.202	6.40	2.76	4.90
TP_5	0.80	0.302	0.346	0.203	6.93	3.12	5.67	0.293	0.340	0.186	6.94	3.10	5.70	0.306	0.362	0.200	7.08	3.15	5.65
TP_6	0.95	0.326	0.377	0.222	7.58	3.50	6.36	0.324	0.377	0.199	7.60	3.50	6.37	0.331	0.427	0.214	7.58	3.60	6.33
TP_7	1.10	0.340	0.392	0.225	8.22	3.90	7.06	0.350	0.415	0.221	8.35	3.88	7.11	0.344	0.476	0.214	8.79	3.99	7.02
TP_8	1.25	0.358	0.410	0.238	8.82	4.28	7.72	0.369	0.438	0.235	8.94	4.26	7.78	0.364	0.476	0.236	9.23	4.36	7.67
TP_9	1.40	0.373	0.432	0.250	9.44	4.70	8.44	0.374	0.443	0.252	9.44	4.68	8.43	0.380	0.500	0.248	9.81	4.77	8.40
TP_{10}	1.55	0.377	0.433	0.253	10.05	5.15	9.16	0.395	0.464	0.251	10.05	5.05	9.12	0.393	0.500	0.259	10.39	5.16	9.10
TP_{11}	3.65	0.495	0.500	0.343	17.90	10.67	17.33	0.490	0.500	0.342	17.90	10.65	17.35	0.490	0.500	0.358	17.90	10.68	17.30
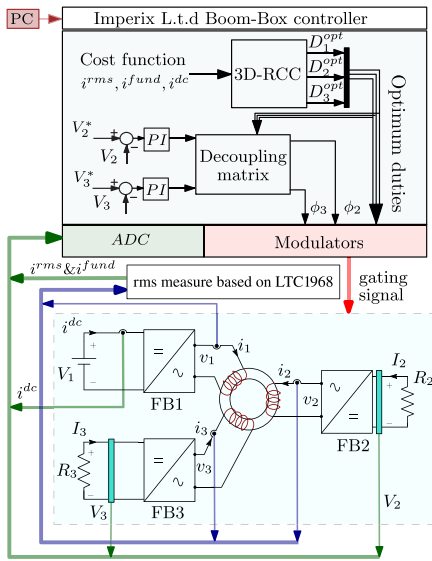
Fig. 7. Structure of the experimental setup.

and port-3 are connected to two dc electronic loads R_2 and R_3, respectively.

The 3D-RCC search together with converter control and modulation is implemented on an Imperix L.t.d. B-Box RCP controller, as done in the previous Section V-A, driving six Imperix PEB8032-A half-bridges. Values of rms quantities are obtained by a signal conditioning circuit based on the integrated circuit LTC1968 by Analog Devices.

A total of 11 points are tested at different loads. The test cases are chosen to represent voltage mismatch case at converter ports with $V_1 = 400$ V, $V_2 = 320$ V, and $V_3 = 480$ V. To obtain different load conditions, port-3 power is changed from low to high power levels while port-2 power is fixed at $P_2 = 350$ W.

For each set-point the correlation search is run considering the minimization of
1) the total true rms current i^{rms};
2) the total fundamental rms current i^{fund};
3) the input dc current i^{dc}.

Herein, three different cost functions are optimized to validate the generic solution found by the proposed 3D-RCC. It is worth

recalling that optimizing the total rms current mainly benefits copper and conduction loss, while optimizing the input dc current allows the optimization of the overall converter loss, including, switching loss, conduction loss, transformer loss, etc. Then, considering the following reported results, input dc-current optimization may lead to lower overall loss while still showing higher total rms current with respect to what obtained by total rms current optimization, which is consistent. The results are summarized in Table IV. The optimal duty-cycles found by the 3D-RCC search are reported as D_1^{opt}, D_2^{opt}, and D_3^{opt}, together with the values of the currents at the found points.

At low-power levels, like at TP1, TP2, and TP3, different final points are obtained as total rms, fundamental, or dc currents are considered as cost variables. This is expected: at low-power levels the optimal duty-cycles are small, which increases the harmonic content of the converter currents. Instead, for high-power levels, like for TP11, the optimization of the cost functions gives almost the same optimal duty-cycles since the optimal duty-cycles lie near the saturation limit, which reduces the weight of the harmonics. The results of optimizing each cost function are discussed in the following.

1) Total True RMS Current Optimization: The results of the 3D-RCC optimizing the total true rms current [i.e., i^{rms} in (5)] are compared to the optimal points found by a systematic BF search, as done in Section V-A too.

Fig. 8 reports the results from both the search techniques. Small differences emerge in Fig. 8(a), (b), and (c) comparing the duty-cycles found by the two different approaches. Fig. 8(d) shows the quantity i^{rms} of the search methods, including also the results by the simple PSM. The proposed 3D-RCC reduces i^{rms} by about 50% in some test cases as compared to PSM. The comparison between the 3D-RCC and the BF results shows the ability of the proposed 3D-RCC to find the true optimum operating point considering the minimization of i^{rms}, with a maximum deviation $< 5\%$.

Fig. 9 shows the dynamic response of the 3D-RCC search optimizing i^{rms} for TP1 of Table IV. The algorithm is started at initial duty-cycles values all equal to 0.4 [see Fig. 9(b)], for which i^{rms} amounts to about 10 A [see Fig. 9(a)]. The proposed 3D-RCC finds the optimum duty-cycles at $D_1^{\text{opt}} = 0.21$, $D_2^{\text{opt}} =$
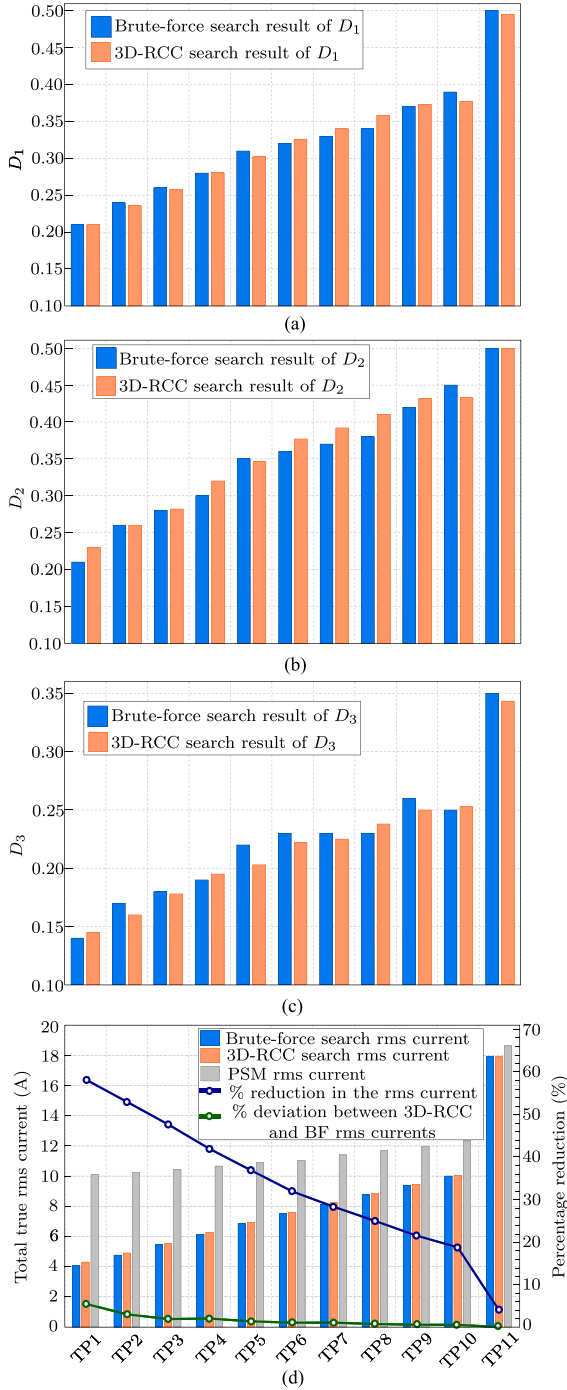
Fig. 8. Results while optimizing total true rms current i^{rms}. (a)–(c) Duty-cycles obtained by the proposed 3D-RCC versus a BF search; (d) rms current with 3D-RCC, BF, PSM.

Fig. 9. Dynamic response of 3D-RCC search optimizing the true rms current i^{rms} of TP1. (a) Total true rms current. (b) Duty-cycles.

the current waveforms in Fig. 10(b), (d), and (f) with the corresponding results by the 3D-RCC reported in Fig. 10(d), peak current values appear substantially reduced for all the three ports.

2) Input DC-Current Optimization: The results of 3D-RCC optimizing the input dc current (i.e., i^{dc}) are now considered. Remarkably, being the voltage at port-1 fixed as well as the power absorbed at port-2 and port-3, such an optimization minimizes the total conversion loss, which includes the sum of conduction and switching loss, of the converter in Fig. 7, because it minimizes the supply current at port-1.

Fig. 11(a) compares the obtained input dc-current by 3D-RCC and PSM. At low-power levels, 3D-RCC reduces the input current by about 30% as compared to PSM. Fig. 11(b) reports the percentage reduction of the converter total loss, showing a reduction > 70% for most of the test cases.

Fig. 12(a) and (b) shows the dynamics of the 3D-RCC recorded during operation at TP9, similar results would be obtained considering other test points. The search starts with initial duty-cycles values set to 0.4 [see Fig. 12(a)] with input dc-current and total converter loss equal to about $5.15\,\text{A}$ and $300\,\text{W}$, respectively [see Fig. 12(b)]. The 3D-RCC finds the optimum point at duty-cycles $D_1^{\text{opt}} = 0.37$, $D_2^{\text{opt}} = 0.44$, and $D_3^{\text{opt}} = 0.25$, where the input dc-current and total loss decrease to approximately $4.68\,\text{A}$ and $122\,\text{W}$, respectively. The input dc-current optimization reduces the overall loss by about 60% with respect to the conditions at the starting point.

Although total converter loss minimization does not imply, in general, soft-switching conditions for all the converter switches, a correlation between the two may easily emerge. Fig. 13 shows what was obtained from this respect with the considered converter in Fig. 7, operating at TP9 with PSM and 3D-RCC. With the currents and voltages directions indicated in Fig. 7, soft-switching conditions at devices turn-ON (ZVS) are assumed at a port if i) a rising voltage transition occurs with negative port current ii) a falling voltage transition occurs with positive port

0.23, and $D_3^{\text{opt}} = 0.145$ with $i^{\text{rms}} \approx 4.2\,\text{A}$, thus reducing the total true rms current by about 58% of its original value.

Fig. 10 shows the transformer voltage and current waveforms at TP1 with different modulation approaches. Fig. 10(a) and (b) shows the converter waveforms with duty-cycles all at 0.4 before starting 3D-RCC, which, after being activated, brings to the steady-state operation displayed in Fig. 10(c) and (d), the optimal duty-cycles found are reported in Fig. 9(b). Fig. 10(e) and (f) displays the converter waveforms with PSM. Comparing
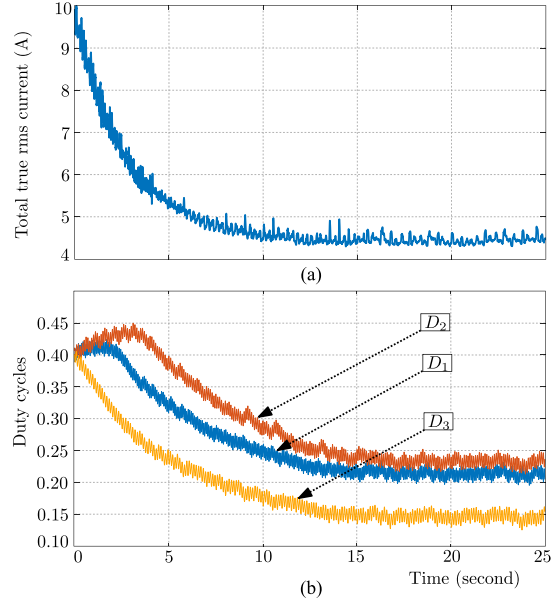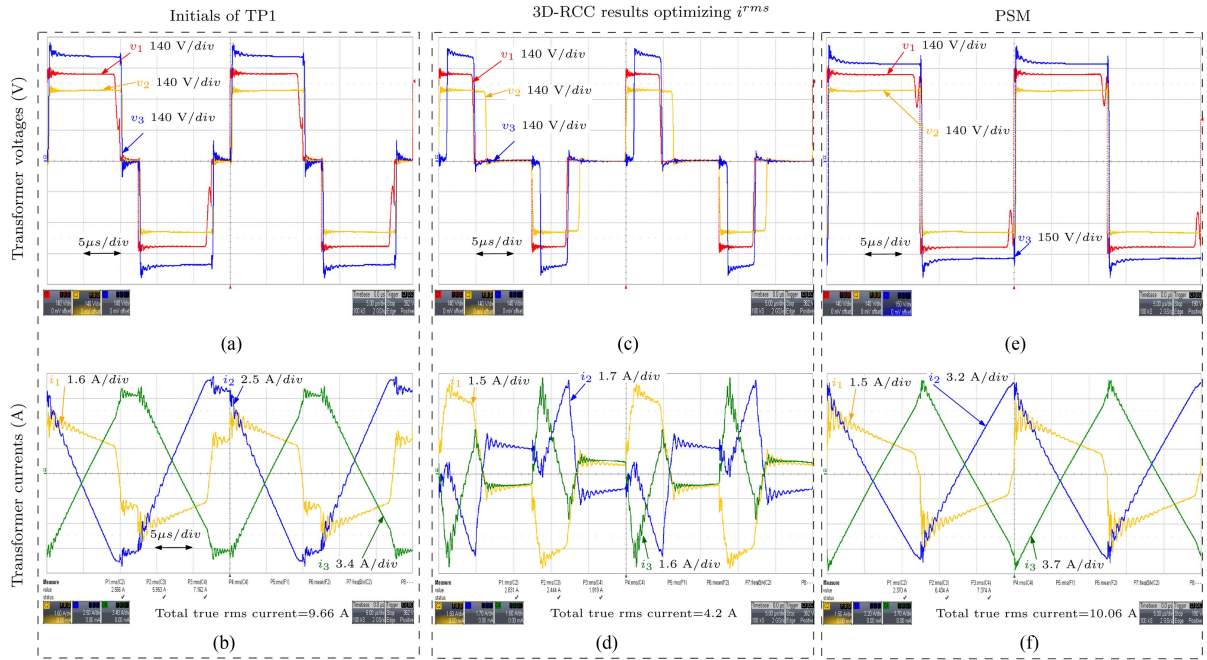
Fig. 10. Experimental waveforms at TP1, (a) and (b) before and (c) and (d) after 3D-RCC optimizing i^{rms}; (e) and (f) with PSM.
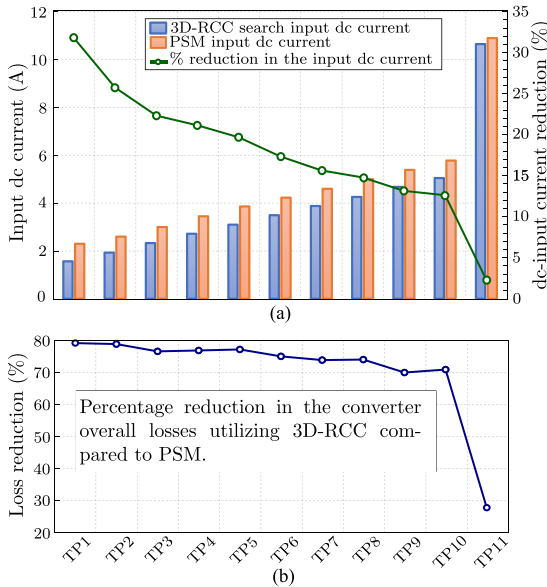

Fig. 11. Results while optimizing the input dc current i^{dc}. (a) input dc current with 3D-RCC versus PSM. (b) Total loss reduction.

current [29]. Then, Fig. 13(a) shows ZVS for port-1 and port-3 switches, while the conditions are not met for the switches of port-2. Fig. 13(b) reports the results from the proposed 3D-RCC method, showing that the switches of port-2, in addition to those of port-1 and port-3, experience soft switching. Besides, 3D-RCC optimization also reduced the switched current values, which also contributes to decreasing the overall converter loss.

3) Total Fundamental Rms Current Optimization: The proposed 3D-RCC is used in this part to optimize the fundamental component of the total true rms current (i.e., i^{fund}). This
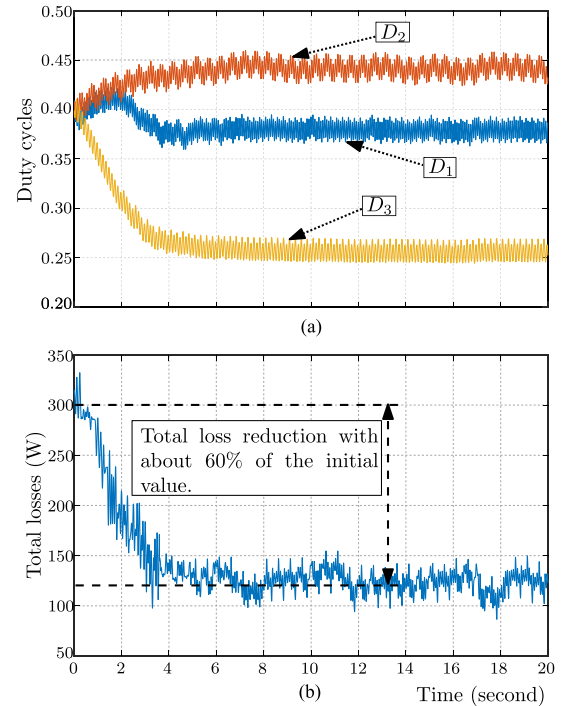

Fig. 12. Dynamic response of 3D-RCC search optimizing the input dc current i^{dc} of TP9. (a) Duty-cycles. (b) Total loss.

practice mainly illustrates that the proposed method is generic regarding optimizing different cost functions. Fig. 14 shows the fundamental rms current of the 3D-RCC compared to the fundamental current of the PSM technique, with a reduction up to about 70% in one of the test cases.
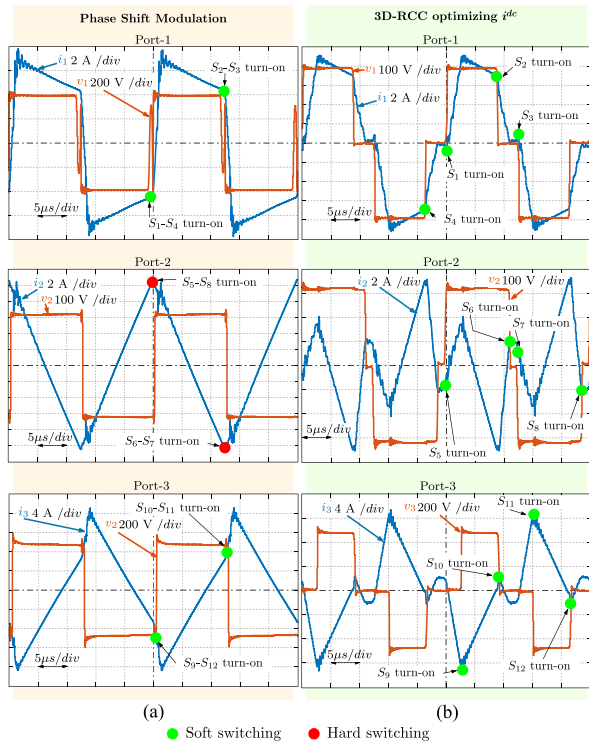
Fig. 13. Experimental ports voltages and currents at TP9 with soft and hard switching transitions indicated; (a) with PSM and (b) after applying the proposed 3D-RCC with i^{dc} optimization.
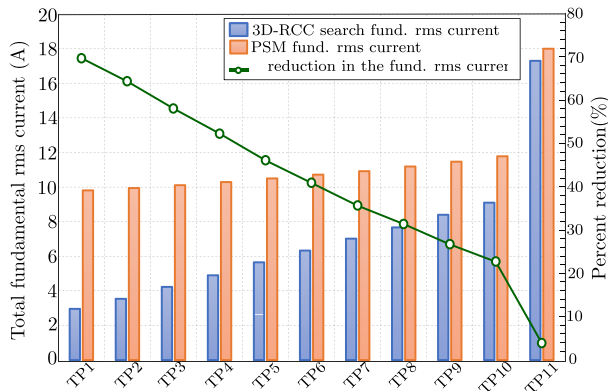

Fig. 14. Total fundamental rms current of the proposed 3D-RCC optimizing i^{fund} versus PSM.

Table I compares the proposed 3D-RCC and other optimization techniques reported in the literature, showing the advantage of the proposed technique of providing an online model-free optimization technique that can be adjusted to optimize different cost functions.

In summary, besides the consistency of the obtained results with what expected considering TAB specific application, the experimental validation showed the effectiveness and robustness of the proposed 3D-RCC approach for multidimensional converter optimization. As a final remark, even though various cost functions (i.e., i^{rms}, i^{fund}, and i^{dc} in Fig. 3) are considered herein to show the flexibility of 3D-RCC in solving different optimization targets, dc-current minimization requires only the

measurement of dc currents to be performed and should be preferred for overall loss minimization.

VI. CONCLUSION

The operation of the ripple correlation technique has been shown considering the multidimensional problem of minimizing the conversion loss of a TAB converter. Optimal TAB modulation is a complex task, given the many variables concurring in the converter operation. Considering typical modulation schemes, five variables are available for control, that is, two phase-shifts and three duty-cycles. This article shows that a multidimensional correlation search can be adopted to tackle the challenge of finding optimal modulation parameters. The proposed method makes use of an orthogonal perturbation signal for each degree of freedom available for optimization. Then, the modulation parameters are adjusted on the basis of the correlation among the orthogonal signal and the corresponding perturbation found on the variable chosen for optimization. Orthogonality can be achieved by using sinusoidal perturbations of different frequencies. The method—which is performed online and does not require the knowledge of converter parameters, namely, it is model-free—shown general validity in the considered application: it is capable of finding appropriate modulation parameters considering various quantities for optimization, such as total rms, dc, or fundamental currents exchanged at the port of the converter. Experimental results show the effectiveness of the proposed online model-free approach for the optimal operation of the TAB.

REFERENCES

[1] M. Rashidi, N. N. Altin, S. S. Ozdemir, A. Bani-Ahmed, and A. Nasiri, "Design and development of a high-frequency multiport solid-state transformer with decoupled control scheme," *IEEE Trans. Ind. Appl.*, vol. 55, no. 6, pp. 7515–7526, Nov./Dec. 2019.

[2] H. V. M., C. Kumar, and M. Liserre, "An MVDC based meshed hybrid microgrid enabled using smart transformers," *IEEE Trans. Ind. Electron.*, vol. 69, no. 4, pp. 3722–3731, Apr. 2021.

[3] F. Vaca-Urbano and M. S. Alvarez-Alvarado, "Power quality with solid state transformer integrated smart-grids," in *Proc. IEEE PES Innov. Smart Grid Technol. Conf. Latin America*, 2017, pp. 1–6.

[4] M. A. Rahman, M. R. Islam, K. M. Muttaqi, and D. Sutanto, "Design of a multiloop control structure for load-disturbance attenuation and power-mismatch mitigation in isolated multiport power converters," *IEEE Trans. Ind. Electron.*, vol. 69, no. 9, pp. 8984–8996, Sep. 2022.

[5] F. Krismer and J. W. Kolar, "Closed form solution for minimum conduction loss modulation of DAB converters," *IEEE Trans. Power Electron. Power Electron.*, vol. 27, no. 1, pp. 174–188, Jun. 2012.

[6] T. Pereira, F. Hoffmann, R. Zhu, and M. Liserre, "A comprehensive assessment of multiwinding transformer-based DC–DC converters," *IEEE Trans. Power Electron.*, vol. 36, no. 9, pp. 10020–10036, Sep. 2021.

[7] R. W. De Doncker, D. M. Divan, and M. H. Kheraluwala, "A three-phase soft-switched high-power-density DC/DC converter for high-power applications," *IEEE Trans. Ind. Appl.*, vol. 27, no. 1, pp. 63–73, Jan./Feb. 1991.

[8] C. Zhao and J. W. Kolar, "A novel three-phase three-port UPS employing a single high-frequency isolation transformer," in *Proc. IEEE 35th Ann. Power Electron. Specialists Conf.*, 2004, pp. 4135–4141.

[9] J. L. Duarte, M. Hendrix, and M. G. Simoes, "Three-port bidirectional converter for hybrid fuel cell systems," *IEEE Trans. Power Electron.*, vol. 22, no. 2, pp. 480–487, Mar. 2007.

[10] C. Zhao, S. D. Round, and J. W. Kolar, "An isolated three-port bidirectional DC-DC converter with decoupled power flow management," *IEEE Trans. Power Electron.*, vol. 23, no. 5, pp. 2443–2453, Sep. 2008.

[11] P. Purgat, S. Bandyopadhyay, Z. Qin, and P. Bauer, "Zero voltage switching criteria of triple active bridge converter," *IEEE Trans. Power Electron.*, vol. 36, no. 5, pp. 5425–5439, May 2021.

[12] J. Li, Q. Luo, T. Luo, D. Mou, and M. Liserre, "Efficiency optimization scheme for isolated triple active bridge DC-DC converter with full soft-switching and minimized RMS current," *IEEE Trans. Power Electron.*, vol. 37, no. 8, pp. 9114–9128, Aug. 2022.

[13] S. Dey and A. Mallik, "Multivariable-modulation-Based conduction loss minimization in a triple-active-bridge converter," *IEEE Trans. Power Electron.*, vol. 37, no. 6, pp. 6599–6612, Jun. 2022.

[14] S. Dey, A. Mallik, and A. Akturk, "Multi-variable multi-constraint optimization of triple active bridge DC-DC converter with conduction loss minimization," in *Proc. IEEE Appl. Power Electron. Conf. Expo.*, 2022, pp. 355–360.

[15] A. Chandwani and A. Mallik, "Three-loop multi-variable control of triple active bridge converter with power flow optimization," in *Proc. IEEE Appl. Power Electron. Conf. Expo.*, 2022, pp. 2008–2013.

[16] I. Kougioulis, P. Wheeler, and M. R. Ahmed, "An integrated on-board charger and AuxiliaryPower module for electric vehicles," in *Proc. IEEE Appl. Power Electron. Conf. Expo.*, 2022, pp. 1162–1169.

[17] R. Yapa and A. Forsyth, "Extended soft switching operation of the triple active bridge converter," in *Proc. 6th IET Int. Conf. Power Electron. Mach. Drives*, 2012, pp. 1–6.

[18] Y. H. Lim and D. Hamill, "Synthesis, simulation and experimental verification of a maximum power point tracker from nonlinear dynamics," in *Proc. IEEE 32nd Ann. Power Electron. Specialists Conf.*, 2001, pp. 199–204.

[19] J. W. Kimball and P. T. Krein, "Discrete-time ripple correlation control for maximum power point tracking," *IEEE Trans. Power Electron.*, vol. 23, no. 5, pp. 2353–2362, Sep. 2008.

[20] T. Esram, J. Kimball, P. T. Krein, P. L. Chapman, and P. Midya, "Dynamic maximum power point tracking of photovoltaic arrays using ripple correlation control," *IEEE Trans. Power Electron.*, vol. 21, no. 5, pp. 1282–1291, Sep. 2006.

[21] P. Ahlgren et al., "Requirements for a cocitation similarity beasure, with special reference to Pearson's correlation coefficient," *J. Amer. Soc. Inf. Sci. Tech.*, vol. 54, no. 6, pp. 550–560, 2003.

[22] K. Ariyur and M. Krstić, *Real-Time Optimization by Extremum-Seeking Control*. New York, NY, USA: Wiley, 2003.

[23] M. Krstić and H.-H. Wang, "Stability of extremum seeking feedback for general nonlinear dynamic systems," *Automatica*, vol. 36, no. 4, pp. 595–601, 2000.

[24] X. Wu, J. Zeng, A. Tagliabue, and M. W. Mueller, "Model-free online motion adaptation for energy-efficient flight of multicopters," *IEEE Access*, vol. 10, pp. 65507–65519, 2022.

[25] W. Wang and W. Zhang, "Intelligent reflecting surface configurations for smart radio using deep reinforcement learning," *IEEE J. Sel. Areas Commun.*, vol. 40, no. 8, pp. 2335–2346, Aug. 2022.

[26] X. Lu, M. Krstić, T. Chai, and J. Fu, "Hardware-in-the-loop multiobjective extremum-seeking control of mineral grinding," *IEEE Trans. Control Syst. Technol.*, vol. 29, no. 3, pp. 961–971, May 2021.

[27] H. Cao, G. Zhu, F. Diao, and Y. Zhao, "Novel power decoupling methods for three-port triple-active-bridge converters," in *Proc. IEEE Appl. Power Electron. Conf. Expo.*, 2022, pp. 1833–1837.

[28] A. Karbozov, M. Ghosh Majumder, H. Krishnamoorthy, and K. Rajashekara, "Medium frequency SST based multiport energy routers for subsea-renewable interconnection," in *Proc. IEEE Appl. Power Electron. Conf. Expo.*, 2022, pp. 416–421.

[29] Y. Wu et al., "A 150-kW 99 all-silicon-carbide triple-active-bridge converter for solar-plus-storage systems," *IEEE Trans. Emerg. Sel. Topics Power Electron.*, vol. 10, no. 4, pp. 3496–3510, Apr. 2022.

Tommaso Caldognetto (Senior Member, IEEE) received the M.S. (Hons.) degree in electronic engineering and the Ph.D. degree in information engineering from the University of Padova, Padova, Italy, in 2012 and 2016, respectively.

He is currently an Assistant Professor with the Department of Management and Engineering, University of Padova, Vicenza, Italy. His research interests include the control of grid-tied converters, microgrid architectures, converters for dc nanogrids, and real-time simulation for power electronics applications.

Davide Biadene (Member, IEEE) received the M.S. degree in electronic engineering and the Ph.D. degree in information engineering from the University of Padova, Padova, Italy, in 2014 and 2017, respectively.

He is currently a Research Fellow with the Department of Management and Engineering, University of Padova, Vicenza, Italy. He was a Visiting Ph.D. Student with the Power Electronic Systems Laboratory, Department of Information Technology and Electrical Engineering, ETH Zurich, Zurich, Switzerland, in 2016. His current research interests include dc–dc converters for renewables and energy storage devices.

Paolo Mattavelli (Fellow, IEEE) received the M.S. (Hons.) and Ph.D. degrees in electrical engineering from the University of Padova, Padova, Italy, in 1992 and 1995, respectively.

He is currently a Full Professor with the University of Padova. His current Google scholar H-index is 80. His major research interests include analysis, modeling, and analog and digital control of power converters, grid-connected converters for renewable energy systems and microgrids, and high-temperature and high-power-density power electronics.

Dr. Mattavelli was an Associate Editor for the IEEE TRANSACTIONS ON POWER ELECTRONICS from 2003 to 2012. He is a Co-Editor-in-Chief for the IEEE TRANSACTIONS ON POWER ELECTRONICS. From 2005 to 2010, he was the Industrial Power Converter Committee Technical Review Chair for the IEEE TRANSACTIONS ON INDUSTRY APPLICATIONS. For terms 2003–2006, 2006–2009, and 2013–2015, he was a member-at-large of the IEEE Power Electronics Society's Administrative Committee. He was a recipient of the Prize Paper Award in the IEEE TRANSACTIONS ON POWER ELECTRONICS in 2005, 2006, 2011, and 2012, and the 2nd Prize Paper Award at the IEEE Industry Applications Society Annual Meeting in 2007.

Ahmed A. Ibrahim (Student Member, IEEE) received the B.Sc. degree in electrical engineering and the M.S. degree in power electronics from the Department of Electrical Engineering (Power and Machines Section), Faculty of Engineering, Alexandria University, Alexandria, Egypt, in 2014 and 2018, respectively. He is currently working toward the second-year Ph.D. degree in mechatronics and product innovation engineering with the Department of Management and Engineering, University of Padova, Vicenza, Italy.

His research interests include dc–dc converters for microgrid applications, real-time simulation of power electronics, and modulation of power converters.